



RESEARCH ARTICLE

# A study on the mixing and infrared signal characteristics of a lobed mixer in a micro turbojet engine

C. Lee  and S.M. Choi 

Jeonbuk National University, Jeonju, Jeonbuk, South Korea

**Corresponding author:** S.M. Choi; Email: [csman@jbnu.ac.kr](mailto:csman@jbnu.ac.kr)

**Received:** 15 October 2023; **Revised:** 12 April 2024; **Accepted:** 11 December 2024

**Keywords:** lobed mixer; mixing mechanism; exhaust plume; infrared signature; micro turbojet engine

## Abstract

In this study, measurements and numerical analyses of the temperature distribution of exhaust gas passing through two types of mixers using a micro turbojet engine were performed to investigate the flow mixing performance based on the shape of the mixer, which mixes the bypass air and core air in a gas turbine turbofan engine. To study the mixing characteristics of the mixer, compressed air was supplied through an external duct mounted on a micro turbojet engine to simulate bypass flow, and a system in which hot gas and compressed air were mixed and ejected into the atmosphere was fabricated. A confluent-type mixer and a mixer with 8-lobed mixer channels in the form of a sine wave were used for the experiment. The exhaust gas temperature was measured based on the distance from the nozzle outlet at bypass ratios of 0.5, 1.0 and 1.4. The results showed that the lobed mixer is more effective than the confluent mixer in lowering the exhaust gas temperature as the bypass ratio increased. Numerical analysis results indicated that, in the case of the confluent mixer, flow mixing is primarily performed by shear flow owing to the velocity difference between the core gas and the bypass air. In contrast, in the case of a lobed mixer, flow mixing is achieved through rotational motion and transverse flow. In addition, when the number of lobe channels increased from 8 to 12, the rotational motion increased and the mixing performance improved. Furthermore, infrared signal calculation results confirmed that, as the number of lobe channels increased, improved flow mixing effectively reduced the infrared signal. We conclude that this study helps understand the mixing characteristics of the flow according to the shape of the mixer at various bypass ratios and determine their effect on the characteristics of the infrared signal.

## Nomenclature

MTE      micro turbojet engine  
BP        bypass ratio

## Symbols

Re        Reynolds number  
Pe        penetration of the lobe  
 $h$         height of the lobe (mm)  
 $L_m$       length of the lobe (mm)  
 $u, v, w$     velocity components in  $(x, y, z)$  (m/s)  
 $\mu_t$       turbulent viscosity (pa·s)  
 $\eta$         thermal mixing efficiency  
 $\rho$         density ( $\text{kg/m}^3$ )  
 $V$         velocity (m/s)  
 $\bar{u}_t$       transverse velocity (m/s)  
 $D$         nozzle diameter (mm)

$\omega_x$	streamwise vortices
T	temperature (°C)
$\dot{m}$	mass flow rate (kg/s)
$Y_j$	local mass fraction of the species
$\bar{J}_i$	diffusion flux of the species
$d_i$	turbulent diffusivity
$i_b(l)$	black body intensity
$i_b(l)$	average incident intensity with respect to the wavelength; plank blackbody intensity
$i'_\lambda$	spectral intensity (w/m <sup>2</sup> /μm/sr)
$a_i(l)$	incident mean
$a_p(l)$	plank mean
$a_\lambda(l)$	spectral absorption coefficient
$\Omega$	solid angle (°)
$\Lambda$	wavelength (μm)
$\kappa_\lambda$	optical thickness
$\varepsilon$	dissipation rate
K	kinetic energy
p	pressure
F	thrust
$A_{\text{exit}}$	nozzle exit area

## 1.0 Introduction

The mixer used in a gas turbine propulsion engine is a fluid dynamics device developed to enhance the mixing performance of fluids. In the field of aviation, mixers are used to reduce noise and specific fuel consumptions [1]. Recently, as interest in and the necessity for stealth technology has increased, attention has been paid to the infrared-signal reduction effect of the mixer. In the turbofan engine's exhaust system, Shan et al. [2] found that the infrared radiation from the plume decreased by 40% when using a lobed forced mixer with a bypass ratio of 1.0, in comparison to a confluent mixer. Similarly, Choi et al. [3, 4] observed that the infrared signal from a lobed mixer was reduced by 30.6% for the same bypass ratio, when compared to a cone nozzle. For this purpose, a mixer is used to improve the flow mixing performance of the bypass flow and core gas. Research has long been conducted to identify the design variables that can improve the mixing performance of mixers and understand the mixing process mechanism. Presz et al. [5] conducted a study, which showed that a mixer ejector diffuser system is effective in improving thrust performance and suppressing noise. Peterson [6] explained the presence of large-scale vortices in the flow induced by the special geometry of a lobed mixer and concluded that the generated large-scale vorticity improved the mixing performance. Tew et al. [7] described that the efficiency of streamwise vorticity decreases as the lobe height-to-wavelength ratio increases and that at higher height-to-wavelength ratios there is a net performance penalty associated with the addition of streamwise vorticity. Abolfadl et al. [8] studied the effect on the mixing process downstream of the trailing edge by varying the height, wavelength and penetration angle of the lobed mixer. Hu et al. [9] described the flow mixing process in detail using a particle image velocimetry system. McCormick and Bennett [10] utilises flow visualisation techniques to analyse the flow patterns and mixing behaviour of different lobed mixer configurations, offering valuable insights for design optimisations. Merati and Cooper [11] used particle image velocimetry and laser induced fluorescence techniques to measure the flow of different mixers. Eckerle et al. [12] and Yu [13] used laser doppler velocimetry (LDV) to measure the flow field downstream of the trailing edge of a lobed mixer. Tsui et al. [14] described a numerical calculation procedure for the flow analysis of a mixer. Sheng et al. [15, 16] evaluated the mixing performance of lobed mixers with various shapes using numerical analysis and explained the dynamics of the mixing process. Meslem et al. [17] presented investigation of flow in a turbulent isothermal air lobed jet. The high entrainment rates are concurrently regulated by the turbulent structures induced by the nozzle's asymmetric shape. The lobed forced mixer has the advantage of infrared suppression for the turbo-fan engine. Therefore, the infrared (IR) radiation suppression for lobed mixers have been investigated by

analytical studies in the past. Lockwood and Shah [18] developed a discrete transfer method for thermal radiation analysis of combustors. Cheng et al. [19] studied investigation of the effect of engine swirl on the infrared signature of the serpentine nozzle. The engine swirl mainly contributed to the infrared signature suppression from the gas. Decher [20] analysed infrared radiation emission for a mixed turbofan engine. He pointed out that the increase in IR emissions due to afterburning was significantly larger than the corresponding increase in thrust.

In addition, research using rig experimental devices is being conducted by several researchers. Liu [21] presents experimental results on the performance of lobed mixer in various mixer designs and discusses the analysis of mixing efficiency. Elliott et al. [22] combines numerical simulation with experimental data to analyse the flow numerical simulations with experimental data to analyse the flow characteristics and mixing performance of lobed mixers, providing insights into their design and optimisation.

However, little experimental study using actual gas turbine engine has been conducted due to difficulties in the preparation process, and there are limitations in that most of the previous studies present results from analytical methods or research using rig devices in laboratories. This study aims to analyse the effects of simulating the characteristics of real engines by mixing the high-temperature core gases, combusted by kerosene fuel, with bypass air in the mixer after passing through the rotating turbine. Through this research, we hope to understand the effects in real engines that were not clear in previous studies. Therefore, in this study, numerical analyses of the temperature distribution of exhaust gas passing through two types of mixers using a micro turbojet engine were performed to investigate the flow mixing performance based on the shape of the mixer. The core gas was simulated using a micro turbojet engine, the bypass flow was simulated using external air, and the temperature and flow characteristics of the exhaust gas were measured using confluent and lobed mixers. In addition, the experimental device used in the experiment was applied as a numerical analysis model to compare and analyse the experimental results and evaluate the mixing process before and after applying the mixer. Through these experiments and numerical analyses, the mixing mechanism of the flow before and after the application of the lobed mixer can be understood in more detail. Therefore, in this study, there are difficulties in conducting detailed measurements and analysis at the level of laboratory rig, and this is recognised as a limitation of the study.

## 2.0 Experiment

### 2.1 Experimental equipment

The micro turbojet engine (MTE) used in this study was an AMT Olympus HP engine with a maximum thrust of 230 N, compression ratio of 3.8, maximum revolutions per minute (RPM) of 108,500, and maximum exhaust gas temperature of 750°C. The temperature at the turbine outlet was measured using a temperature sensor mounted on the engine.

A bypass nozzle was fabricated to simulate the flow of a turbofan engine, and its shape is illustrated in Fig. 1. The inlet and outlet diameters ( $D_e$ ) of the bypass nozzle were 117.6 and 92mm, respectively, and the length ( $L$ ) of the nozzle was 278mm. The MTE and the nozzle were bolted between the flanges, and the compressed air was discharged into the atmosphere after being mixed with the core flow and moved through the external duct. The bypass nozzle was manufactured using Inconel, which has strong durability against heat. Two types of mixers were used in the experiment: first is the confluent mixer, which has a basic shape that allows the core flow injected from the engine turbine outlet and the bypass air to mix at a certain distance from the outlet. Figure 2 shows the confluent mixer shape and the model image mounted on the MTE engine. The confluent diameter was set to 80.7mm, which is the same as the turbine diameter of the MTE. The mixer was integrated with an external duct and had a flange connecting the bypass nozzle and the engine. Second is the 8-lobed mixer, which was designed with reference to Baber et al. [23]; the shape and dimensions of the mixer are presented in Figs 3 and 4, respectively.

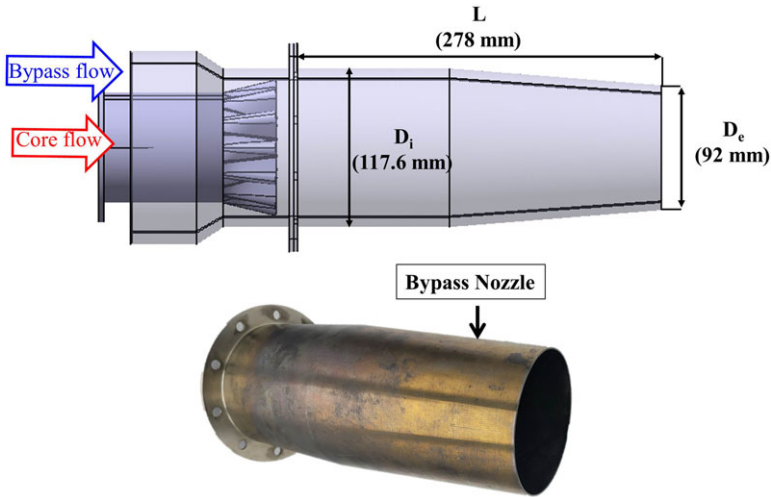


*Figure 1. Bypass nozzle.*

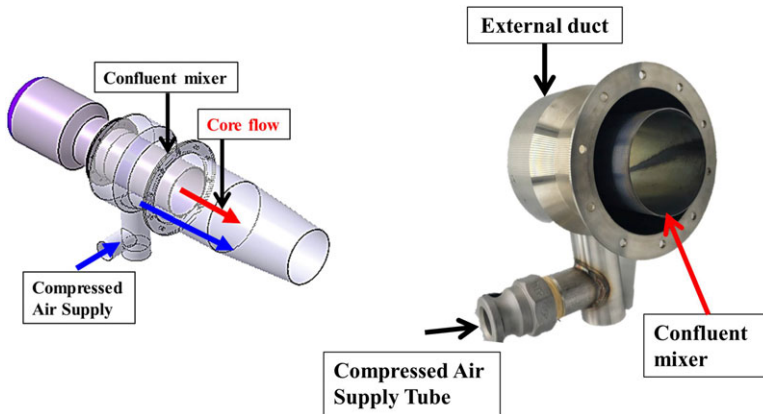


*Figure 2. Confluent mixer.*

The design parameters of the lobe were the height ( $h$ ) and length ( $L_m$ ) of the mixer. Height ( $h$ ) is the protruding length of the lobe, and the mixer length ( $L_m$ ) is the length from the inlet to the outlet of the mixer. Penetration ( $Pe$ ) is the degree of projection to the core and bypass flows, and is defined as the ratio of length to height as follows [4]:

$$Pe = \frac{h}{L_m} \quad (1)$$

The larger the  $Pe$  value, the greater the pressure change, and the more vigorous the distorted flow at the lobe outlet and surface. The  $Pe$  value was set to 0.19 to have the maximum penetration within the range that can be mounted on the MTE. The outer diameter ( $D_o$ ) of lobed mixer was 106 mm, and the inner diameter ( $D_{in}$ ) was 37.6 mm. A photograph of the bypass nozzle and outside air duct mounted on the MTE is shown in Fig. 5. The core gas was generated by the MTE engine, and bypass air joined the core gas through a high-pressure tube. After the core gas and bypass air were mixed, which joined the outside air duct through the mixer, they were sprayed into the atmosphere through the bypass nozzle.

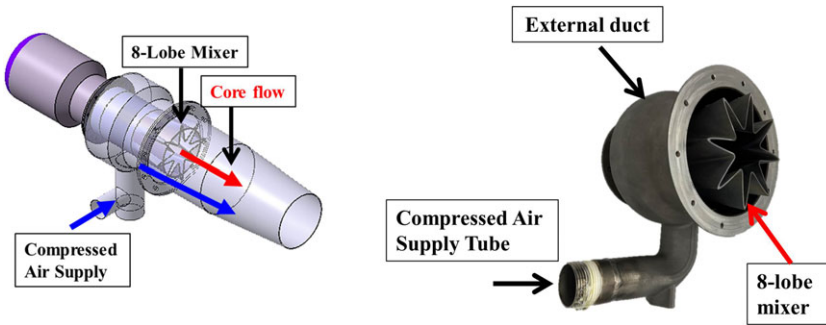


Figure 3. Lobed mixer.

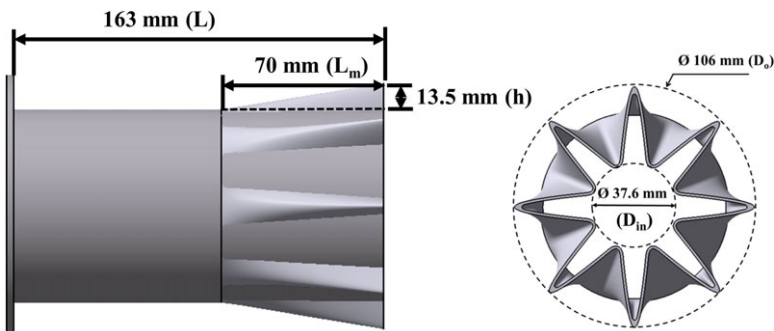


Figure 4. Dimension of the lobed mixer.

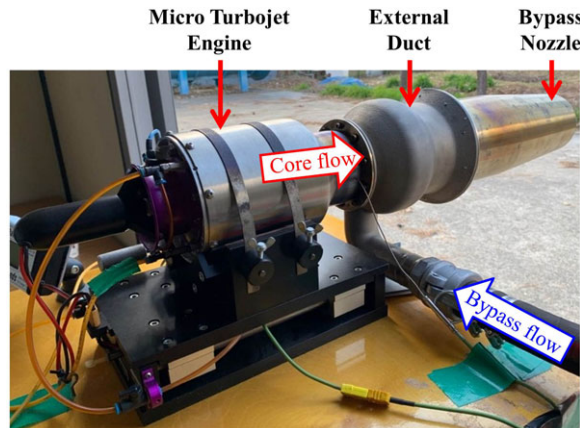
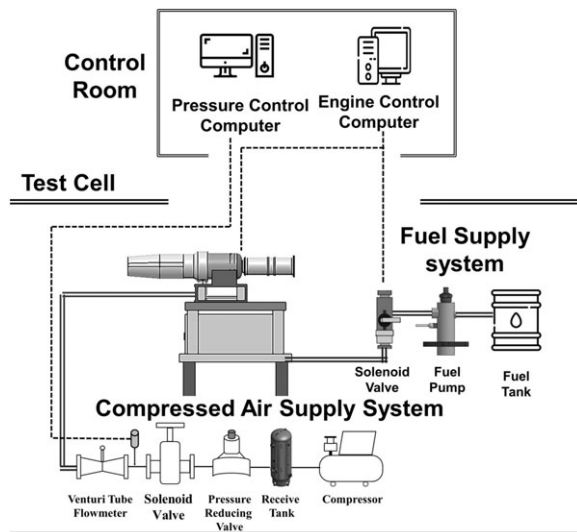


Figure 5. Photo of integrated micro turbojet engine, mixer and bypass nozzle test equipment.

### 2.2 Experimental method

The test setup is shown in Fig. 6. The test equipment consisted of a bypass supply system, control room and fuel supply system. The bypass supply system regulated the flow rate of the high-pressure compressed air and collected the flow measurement data. Compressed air was stored in the receiver tank. When the rotational speed of the RPM sensor located on the impeller blade reached 43,000RPM, through the operation of a solenoid valve located in the engine control room, compressed air was supplied to the



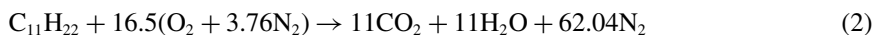
**Figure 6.** Schematic diagrams of the engine test system.

bypass nozzle via a pressure-reducing valve and a venturi tube flow meter. The pressure-reducing valve (DRE-F, YNV) was used to control the flow rate, which was measured using the venturi tube flow meter (GSAV-4000-S; Korea Flow Meter). The temperature of the bypass air supplied to the nozzle was measured using a K-type thermocouple (TJC120-CAXL-062G-2.25, Omega), and the supply pressure was measured using a static pressure sensor (PSPHH0500PCPG, Sensys). The fuel supply device controlled the amount of fuel through an engine control system and consisted of a fuel tank, fuel pump and solenoid valve. The exhaust gas temperature was measured using a traverse system for temperature measurement. The traverse system consisted of a thermocouple and a data-acquisition system. The layout and photographs of the traverse system used to measure the exhaust gas temperature are shown in Figs 7 and 8, respectively. Sixteen thermocouples were mounted at 20-mm intervals to measure a wide range of exhaust gas flow areas. The temperature standard deviation of the 16 thermocouples is  $0.67^{\circ}\text{C}$ , and the accuracy at the 95% confidence level of each thermocouple is  $\pm 1.32^{\circ}\text{C}$ . Data were recorded in real time using NI-cRio 9075 and LabView software, and the position movement was controlled by connecting a PCI card and UMI-7764 to a computer. The exhaust gas temperature was measured at positions  $0.16D_e$ ,  $1D_e$ ,  $2D_e$ ,  $3D_e$ ,  $4D_e$  and  $5D_e$  away from the nozzle outlet. The atmospheric temperature was  $18.6 \pm 3^{\circ}\text{C}$ , and the air pressure was  $1,021.4 \pm 0.9\text{hPa}$  during the test.

### 3.0 Numerical analysis

#### 3.1 Numerical analysis model

The analysis model was used to analyse three nozzle shapes. In addition to the manufactured confluent mixer and the 8-lobed mixer, a 12-lobed mixer was used to compare the changes in the temperature distribution and infrared signal based on the mixer shape. The geometry of the 12-lobed mixer is shown in Fig. 9. The 12-lobed mixer was composed of 12-lobed channels; the lobe width ( $b$ ) was 8mm, and  $Pe$  was 0.25. The boundary conditions of the nozzle consisted of core and bypass inlets. The fuel ( $\text{C}_{11}\text{H}_{22}$ ) in the core region was assumed to be completely burned, and the overall chemical equation of the fuel is as follows:



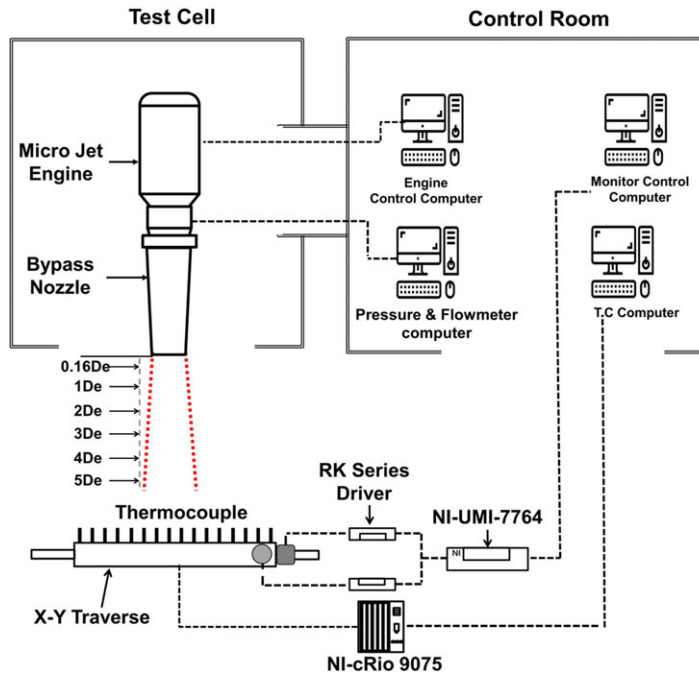


Figure 7. Temperature measuring system.

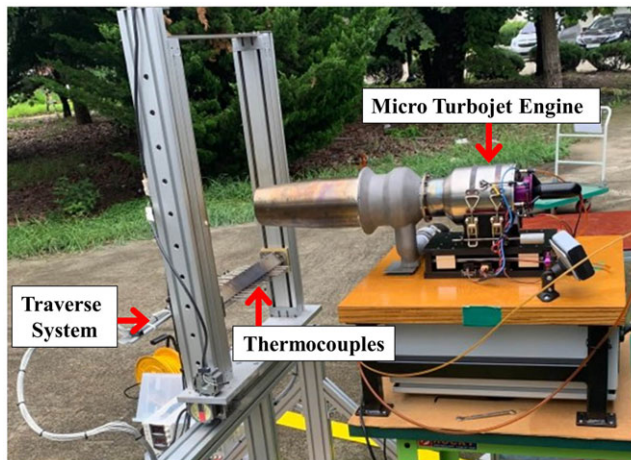


Figure 8. Photo of plume temperature measurement system.

The mole fractions of the exhaust gases produced by combustion were 13.0% and 13.0% for carbon dioxide ( $\text{CO}_2$ ) and water vapour ( $\text{H}_2\text{O}$ ), respectively, and nitrogen ( $\text{N}_2$ ) was composed of chemical species with a mole fraction of 74.0%. We assumed that the external free flow has the same atmospheric properties. The temperature-dependent characteristics of the working fluid are presented in Table 1 [24]. The flow analysis was performed using STAR CCM+ software, in which the equations were discretised with the finite volume method for each control volume.  $k-\varepsilon$  model was adopted in the numerical simulation. A second-order upwind scheme was used for spatial discretisation. In the analysis, the computational fluid governing equations were solved for the mass, momentum and energy conservation using a coupled implicit flow solver where the conservation equations are simultaneously solved as vectors of

**Table 1.** Polynomial coefficients of temperature dependent property [24]

Property (units)	$\alpha_0$	$\alpha_1$	$\alpha_2$	$\alpha_3$	$\alpha_4$	$\alpha_5$
Water vapour (H <sub>2</sub> O)						
$C_p$ (kJ/kg K)	2.3082	6.6923E-5	-7.5368E-6	1.9848E-8	-1.8160E-11	5.7610E-15
$\kappa$ (W/m K)	-1.3898E-2	1.0143E-4				
$\mu$ (N s/m <sup>2</sup> )	-3.0948E-6	4.0724E-8				
Carbon dioxide (CO <sub>2</sub> )						
$C_p$ (kJ/kg K)	0.5117	1.3846E-3	-8.6125E-7	1.9774E-10	2.8525E-15	
$\kappa$ (W/m K)	-1.0992E-2	9.8510E-5	-2.0203E-8			
$\mu$ (N s/m <sup>2</sup> )	9.3761E-7	5.0256E-8	-1.1188E-11			
Nitrogen (N <sub>2</sub> )						
$C_p$ (kJ/kg K)	1.0151	3.4575E-4	-1.8022E-6	4.012E-9	-3.4483E-12	1.0445E-15
$\kappa$ (W/m K)	-0.0011	1.1535E-4	1.1182E-7	1.1353E-10	-6.9355E-14	1.8941E-17
$\mu$ (N s/m <sup>2</sup> )	-3.66E-07	8.18E-08	-9.52E-11	1.02E-13	-6.43E-17	1.71E-20

\*Property =  $\alpha_0 + \alpha_1 \cdot T + \alpha_2 \cdot T^2 + \alpha_3 \cdot T^3 + \alpha_4 \cdot T^4 + \alpha_5 \cdot T^5$ .

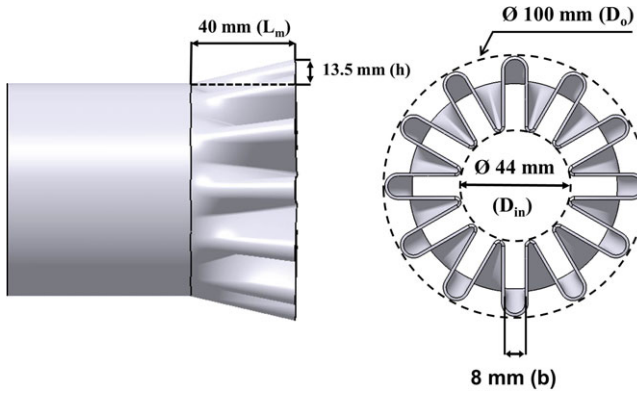


**Figure 9.** 12-Lobed mixer model (CFD).

equations as well as species transport equations included. Reynolds-averaged Navier-Stokes equations were used and the governing equations are expressed as follows:

$$\frac{\partial \rho}{\partial t} + \nabla \cdot (\rho \vec{v}) = 0 \tag{3}$$

$$\frac{\partial}{\partial t} (\rho \vec{v}) + \nabla \cdot (\rho \vec{v} \otimes \vec{v}) = -\nabla \cdot \bar{p}_{mod} I + \nabla \cdot (\bar{T} + T_{RANS}) + f_b \tag{4}$$

$$\frac{\partial}{\partial t} (\rho \bar{E}) + \nabla \cdot (\rho \bar{E} \vec{v}) = -\nabla \cdot \bar{p}_{mod} \vec{v} + \nabla \cdot (\bar{T} + T_{RANS}) \vec{v} - \nabla \cdot \bar{q} + f_b \vec{v} \tag{5}$$

where  $\rho$  is the density of fluid,  $\vec{v}$  is the velocity vector,  $\bar{p}_{mod} = \bar{p} + \frac{1}{2} \rho k$  is the modified mean pressure where  $\bar{p}$  is the mean pressure and  $k$  is the turbulent kinetic energy,  $I$  is the identity tensor,  $f_b$  is the resultant body forces,  $\bar{T}$  is the mean viscous stress tensor,  $\bar{q}$  is the mean heat flow,  $T_{RANS}$  is terms of the mean flow quantities,  $\bar{E}$  is the mean total energy per unit mass.

$$\frac{\partial \rho Y_i}{\partial t} + \frac{\partial}{\partial t} (\rho Y_i) + \nabla \cdot (\rho \vec{v} Y_i) = -\nabla \cdot \vec{J}_i + S_i \tag{6}$$



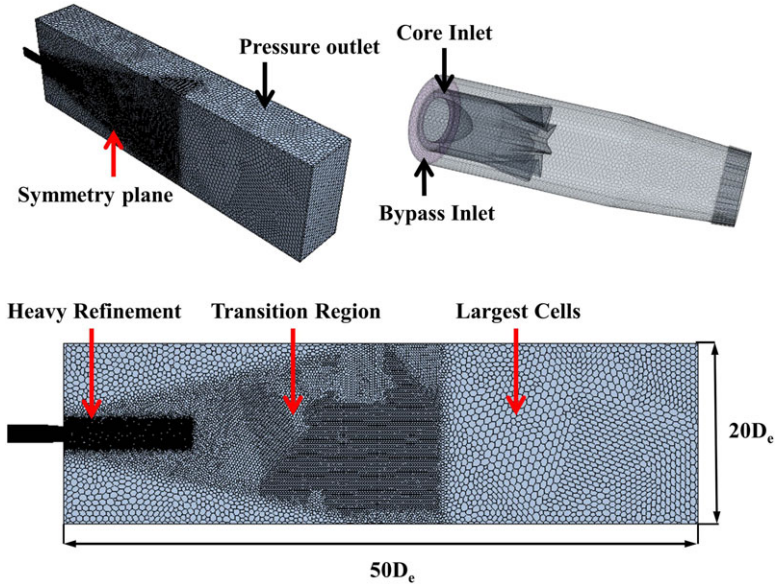


Figure 10. Global computational grid.

where  $\vec{J}_i$  is the diffusion flux for species,  $Y_i$  is the local mass fraction of species, respectively. In a turbulent flow, the mass diffusion is calculated as,

$$\vec{J}_i = -\left(\rho d_i + \frac{\mu_t}{Sc_t}\right) \quad (7)$$

where  $Sc_t$  is the turbulent Schmidt number,  $d_i$  is the turbulent diffusivity, and  $\mu_t$  is the turbulent viscosity. The turbulent (or eddy) viscosity ( $\mu_t$ ) was calculated by combining the kinetic energy ( $k$ ) and the dissipation rate ( $\varepsilon$ ) as follows:

$$\mu_t = c_\mu \rho k^2 / \varepsilon \quad (8)$$

The model constants are  $c_{1\varepsilon} = 1.44$ ,  $c_{2\varepsilon} = 1.92$ ,  $c_\mu = 0.09$ ,  $\sigma_k = 1$ , and  $\sigma_\varepsilon = 1.3$  with the following default values. The  $y+$  wall function technique was used for implementing the boundary layer on the surface.

Grid generation was performed on the half model of the nozzle with symmetry about the Z-axis. The computational domain included the free-stream and downstream exit domains and was  $50D_e \times 20D_e \times 10D_e$ . As shown in Fig. 10, a polyhedral structure with three blocks was created and considerable attention was paid to smooth generation in accordance with the diameter of the high-velocity region of the generated exhaust gas. The nozzle internal Reynolds number was  $1.20 \times 10^5$  and the calculation was performed as follows:

$$\text{Reynolds number (Re)} = \frac{\rho VD}{\mu} \quad (9)$$

Here, the values of the variables, that is, density ( $0.57\text{kg/m}^3$ ), velocity ( $73\text{m/s}$ ), viscosity ( $3.19 \times 10^{-5}\text{Pa} \cdot \text{s}$ ), and diameter ( $92\text{mm}$ ) were used for calculating the Reynolds number. The grid near the nozzle wall had an initial cell height of approximately  $y+ < 1$ . The height of the first grid was  $0.00135\text{mm}$ , and the number of prism layers was 13.

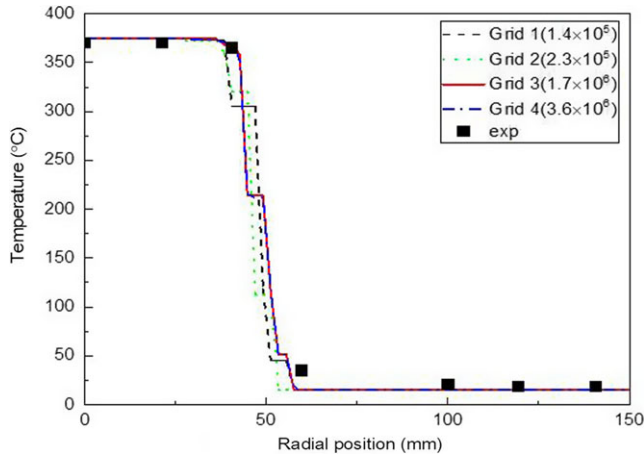


**Figure 11.** Temperature distribution at the  $0.6D_e$  with radial position.

### 3.2 Grid independence and numerical validation

The turbine outlet and bypass air temperatures obtained in the experiment were used as the core and bypass boundary conditions, respectively. The data analysis method used the average recorded data for a certain period after the flow reached a stable state. The average temperature of the turbine used as the boundary condition was  $375^{\circ}\text{C}$  and that of the bypass air was  $29^{\circ}\text{C}$ . The turbine inlet flow rate was  $0.149\text{kg/s}$ , that of the bypass air was 0.5, 1, and 1.4 times the flow rate of the core gas, which varied according to the experimental conditions.

Figure 11 shows the comparison of the experimental results with four computational models at the  $0.16D_e$  position to confirm grid independence. The first stage of the calculation was also performed with a coarser mesh of  $1.4 \times 10^5$  nodes. Finally  $1.7 \times 10^6$  nodes were selected by comparing the temperatures value of the experiment and computational fluid dynamics (CFD). Finer grids would represent the modeled geometry more accurately but restrictions in available computer storage and time impose difficulties in the mesh refinement process.

The temperature distribution results based on the distance of the radial position did not match perfectly when the experimental and analysis results were compared; however, the temperature distribution showed a relatively similar tendency. The coarse grid was  $1.4 \times 10^5$ , the analysis time was 4 hours; the analysis time increased as the number of grids increased. The temperature values converged from the Grid 3 computational model, and Grids 3 and 4 required 32 hours and 54 hours of analysis time, respectively. As a compromise between computing resources and accuracy, Grid 3 was selected in this study. The analysis model was judged to be reliable by verifying the velocity and temperature near the flow rate and nozzle outlet. Therefore, we confirmed that the turbine outlet boundary condition and the analysis model results obtained by measurements in the experiment were valid.

### 3.3 Infrared signal analysis model

The infrared signal of the plume was calculated using the narrowband model. This type of band model represents the average of the radiation properties of each wavelength band [25]. In the case of only absorption and emission without scattering, Infrared signal is calculated based on the radiative heat transfer equation and calculated using a statistical table for the absorption coefficient. Myong et al. [26, 27] performed an infrared signal analysis of the MTE plume using the narrowband approximation method and verified its reliability. The narrowband approximation method can be used to calculate the spectral intensity through the following equation using the heat flow field analysis results, such as the temperature and partial pressure of atmospheric components at a specific point in the plume region:

$$i'_\lambda(l) = i'_{\lambda,\omega} e^{-\kappa_\lambda(l)} + \int_0^{-\kappa_\lambda(l)} i_{b,\lambda}(l^*) \exp[-\kappa_\lambda(l) + -\kappa_\lambda(l^*)] d\kappa_\lambda(l^*) \tag{10}$$

$$\kappa_\lambda = \int_0^l a_\lambda(l^*) dl^* \tag{11}$$

The narrowband approximation method is considered more efficient than the line-by-band model, which requires longer time to compute over a range of infrared wavelengths. The average spectral intensity incident on the differential volume from all directions can be calculated by integrating the spectral intensity over the solid angle  $\Omega$  as follows:

$$\overline{i'_\lambda(l)} = \frac{1}{4\pi} \int i'_\lambda(l) d\Omega \tag{12}$$

In addition, two spectral mean absorption coefficients (incidence and Planck means) were defined.

$$a_i(l) \equiv \frac{1}{i'_i(l)} \int_0^\infty \overline{i'_\lambda(l)} a_\lambda(l) d\lambda, \quad a_p(l) \equiv \frac{1}{i_b(l)} \int_0^\infty \overline{b} = \overline{i_{b,\lambda}(l)} a_\lambda(l) d\lambda \tag{13}$$

In other words, when analysing the infrared signal of the plume, the spectral intensity was calculated using the temperature, pressure and partial pressure values at each point, defined by dividing the line of sight connecting two arbitrary points.

## 4.0 Results and discussion

### 4.1 Plume temperature measurement

Figure 12 shows the exhaust gas temperature distribution when the bypass ratio was 0.5. The figure shows from 0.16D<sub>e</sub> to 5D<sub>e</sub> for each measurement location and is classified by colour for each distance. The confluent mixer is represented by a square symbol, and the 8-lobed mixer is represented by a circular symbol. In addition, 0mm on the lower horizontal axis indicates the centre point of the nozzle. The overall temperature distribution tended to be slightly skewed; however, the difference in values was not large. The exhaust gas temperature decreased as the measurement location was farther from the outlet, and the temperature varied depending on the shape of the mixer. By comparing the temperatures between the mixer configurations, the confluent mixer had maximum exhaust gas temperatures of 343°C and 332°C at the 0.16D<sub>e</sub> and 1.0D<sub>e</sub> positions, respectively. The maximum exhaust gas temperatures of the 8-lobed mixer at the positions of 0.16D<sub>e</sub> and 1.0D<sub>e</sub> were 331°C and 323°C, respectively. The plume temperature reduction rate is defined as the ratio of the plume temperature to the initial turbine outlet temperature (375°C) and is calculated as follows:

$$\text{Temperatuer reduction rate (\%)} = \frac{(\text{Turbine exit temperature} - T_{\max}) \times 100}{\text{Turbine exit temperature}} \tag{14}$$

where  $T_{\max}$  denotes the maximum exhaust gas temperature at the measurement position. The temperature reduction rate at the 0.16D<sub>e</sub> position was 8.5% for the confluent mixer and 11.7% for the 8-lobed mixer. At the 1D<sub>e</sub> location, the temperature reduction rate of the confluent mixer was 11.4% and that of the 8-lobed mixer was 13.8%. At the 2D<sub>e</sub> position, the maximum exhaust gas temperature was lower in the confluent mixer than in the 8-lobed mixer. At this location, the maximum exhaust temperature of the confluent mixer was approximately 285°C, and the maximum exhaust temperature of the 8-lobed mixer was approximately 315°C. The temperature reduction rates were 24% for the confluent mixer and 16% for the 8-lobed mixer.

Figure 13 illustrate the exhaust gas temperature distribution at a bypass ratio of 1.0. By comparing the maximum exhaust gas temperature between mixer configurations, we found that the maximum exhaust gas temperature of the confluent mixer at 0.16D<sub>e</sub> was 325°C (temperature reduction rate, 13.3%) and that of the 8-lobed mixer was 304°C (temperature reduction rate, 18.9%). The maximum exhaust gas temperatures of the confluent mixer at the 3D<sub>e</sub> and 5D<sub>e</sub> positions were 200° (temperature reduction

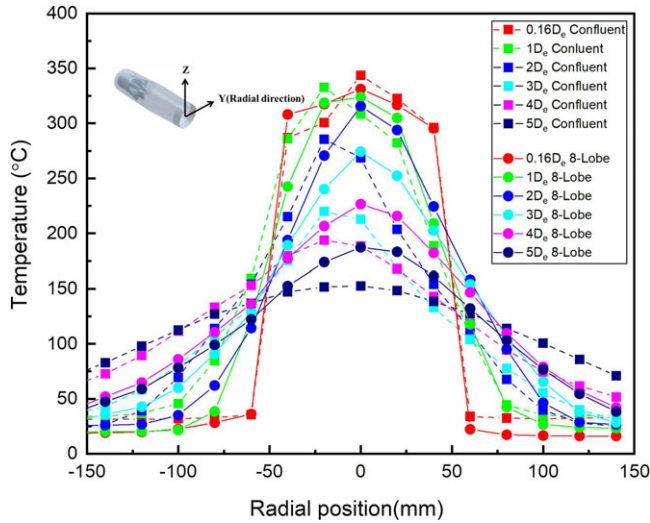


Figure 12. Plume temperature distribution (bypass 0.5).

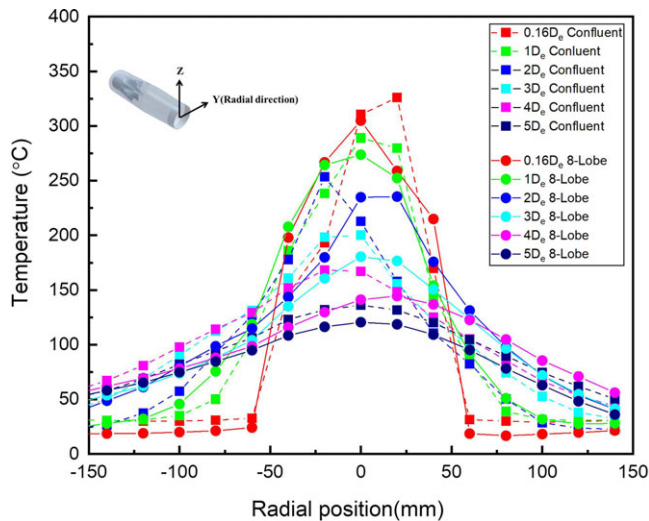


Figure 13. Plume temperature distribution (bypass 1.0).

rate, 46.6%) and 136° (temperature reduction rate, 63.7%), respectively, and those of the 8-lobed mixer were 180° (temperature reduction rate, 52%) and 120° (temperature reduction rate, 68%), respectively. Figure 14 shows the exhaust gas temperature distribution when the bypass ratio is 1.4. In particular, we inferred that the temperature of the 8-lobed mixer significantly decreased at the centre of the nozzle (−20–20mm), and increased flow mixing occurred as the high-pressure compressed air penetrated the core gas. By comparing the maximum exhaust gas temperature, we observed that the maximum exhaust gas temperature of the confluent mixer at 0.16D<sub>e</sub> was 296°C (temperature reduction rate, 21%) and that of the 8-lobed mixer was 244°C (temperature reduction rate, 34%).

To quantitatively express the mixing performance, the thermal mixing efficiencies were compared. Thermal mixing efficiency is an essential factor in mixer design, and jet mixing represents the degree of uniform mixing of the core and bypass flow. The temperature mixing efficiency of the core gas and outside air was based on the results reported by Xie and Liu, and is expressed as follows [28]:

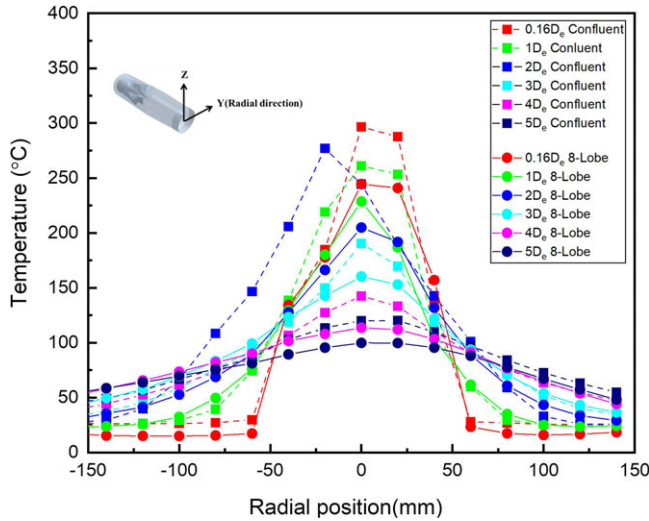


Figure 14. Plume temperature distribution (bypass 1.4).

$$\eta = 1 - \frac{(T_m - T_M)^2 \dot{m}_m}{T_h^2 \dot{m}_h + T_c^2 \dot{m}_c - T_M^2 \dot{m}_m} \tag{15}$$

where  $\dot{m}_m$  is the sum of the flow rates of the hot gas and outside air;  $T_h$  and  $T_c$  are the initial temperatures of the core gas and the external compressed air, respectively; and  $T_M$  is ideally the temperature at which the hot gas and external compressed air are completely mixed.  $T_M$  is defined as follows:

$$T_M = \frac{T_h \dot{m}_h + T_c \dot{m}_c}{\dot{m}_m} \tag{16}$$

In this experiment, the complete mixing temperature was determined according to the bypass airflow rate, and the temperatures at bypass ratios of 0.5, 1.0, and 1.4 were 253.6°C, 197.5°C, and 169.4°C, respectively. The measured average temperature of the exhaust gas region is expressed as follows:

$$T_m = \frac{1}{n} \sum_j T \tag{17}$$

where  $n$  means the number of thermocouples, and the temperature data of thermocouples (−40–40mm) at 0.16 $D_e$  was used. Figure 15 compares mixing efficiencies for different bypass ratios. The thermal mixing efficiency of confluent mixer was 0.980, 0.978 and 0.880 for bypass ratios of 0.5, 1.0 and 1.4. However, in the case of the 8-lobed mixer, thermal mixing efficiency appears to be slightly higher than that of the confluent mixer. The thermal mixing efficiency was 0.982, 0.990 and 0.960 at bypass 0.5 and 1.0 and 1.4. Additionally, the thermal mixing efficiency of the lobed mixer was observed to be higher at a bypass ratio of 1.0 compared to other cases.

### 4.2 Flow and infrared signal analysis

Here, the temperature distributions of the two mixers were compared. Understanding the temperature distribution requires examining the flow of the fluid inside and outside the nozzle. Figures 16, 17 and 18 show the three-dimensional temperature distribution of the internal flow, including the velocity vectors of the three mixers at a bypass ratio of 1.4. The velocity vector used is defined as follows:

$$\vec{u} = u\hat{i} + v\hat{j} + w\hat{k} \tag{18}$$

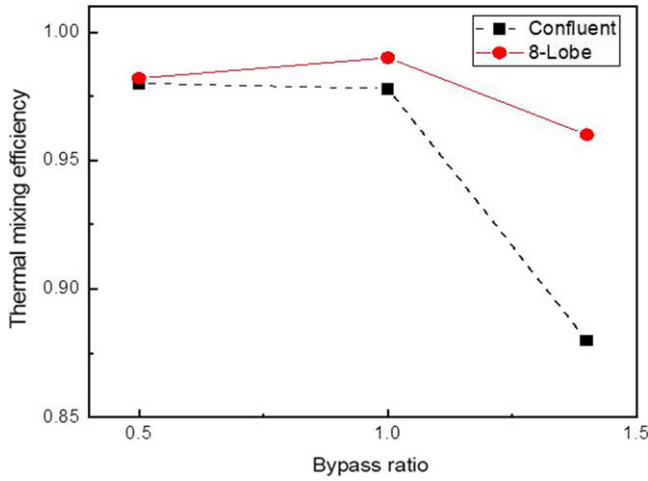


Figure 15. Thermal mixing efficiency with bypass ratio.

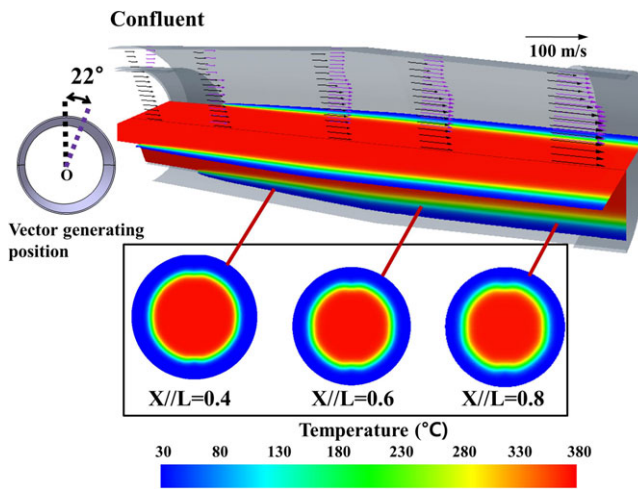


Figure 16. Three-dimensional temperature distributions inside bypass nozzle with confluent mixer.

where  $u\hat{i}$ ,  $v\hat{j}$ , and  $\omega\hat{k}$  are velocity unit vectors corresponding to the  $X$ ,  $Y$  and  $Z$  directions, respectively. In Figs 16, 17 and 18, the black velocity vectors represent the positions on the crests of the lobed mixer, while the purple vectors represent the positions in the troughs of the lobed mixer, extending from the nozzle centre to the bypass duct. Detailed angular information of the vectors is indicated on the left side within each figure. In Fig. 16, for the confluent mixer, it can be seen that the core gas and bypass flow run parallel in the axial direction at the mixer exit. In contrast, in Fig. 18, with the 12-lobed mixer, the black vectors (representing the crest direction of the lobed mixer) flow axially parallel near the nozzle centre but tend toward the outer edge in the direction of the bypass duct, while the purple vectors (representing the trough direction of the mixer) are similar to the black vectors near the nozzle centre but flow towards the nozzle centre as they move outward. Additionally, looking at the temperature distribution, for the confluent mixer, the core gas and bypass flow do not mix, with the bypass flow maintaining an initial temperature of about 30°C. In the case of the 8-lobed mixer, the bypass flow and core gas are not uniformly mixed while flowing from the mixer to the nozzle exit, and a dispersed flow with initial temperatures of 30°C and mixed temperatures of about 200°C can be observed. In the case of the

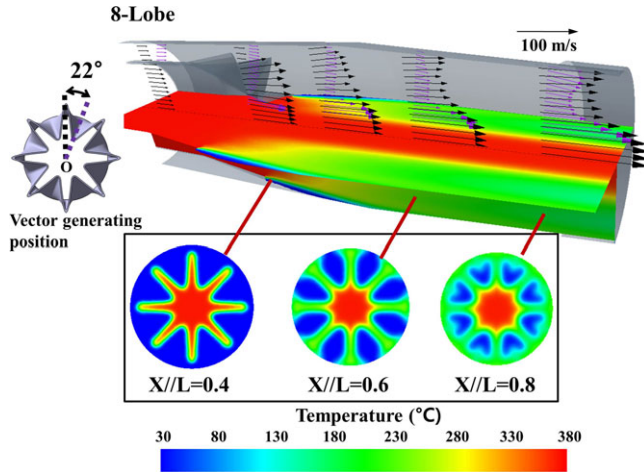


Figure 17. Three-dimensional temperature distributions inside bypass nozzle with 8-lobed mixer.

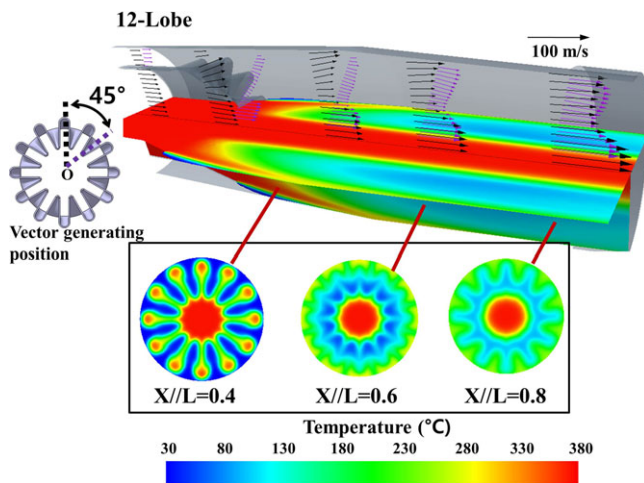
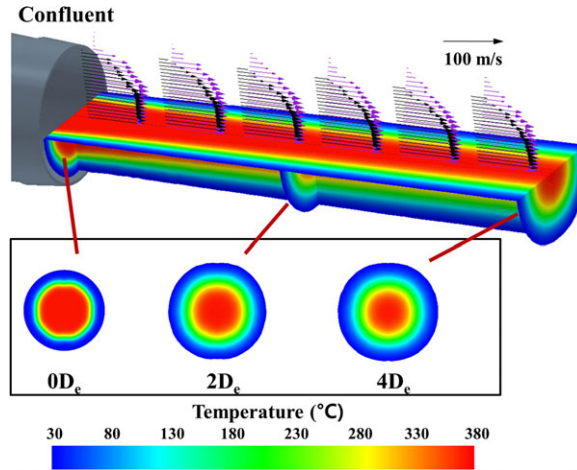


Figure 18. Three-dimensional temperature distributions inside bypass nozzle with 12-lobed mixer.

12-lobed mixer, the bypass flow mixes with the high-temperature area as it flows from the end of the mixer to the nozzle exit, resulting in a uniform temperature distribution of about 200°C. This phenomenon is believed to be due to the increase in the contact area between the core gas and bypass as the number of channels in the lobed mixer increases from 8 to 12, thereby enhancing the mixing effect of the two flows.

As factors enhancing the mixing effect in these lobed mixers, Hu et al. [29] explained that the generation of smaller-scale vortices within the lobed mixers, and deceleration of the central velocity, are contributing factors. That is, in the case of lobed mixers, due to their complex structure, significant disturbances can occur along the azimuthal direction of the jet flow, leading to different flow directions in the crests and troughs. However, the velocity difference between bypass air and core gas acts as a factor enhancing the mixing of each flow, and as it progresses downstream, vortices gradually dissipate, and the velocity distribution becomes increasingly uniform [10, 30].

The temperature and velocity distribution of the plume emitted into the atmosphere from the nozzle exit are presented in Figs 19, 20 and 21, respectively. In the case of the confluent mixer shown in Fig. 19,



**Figure 19.** Three-dimensional temperature distributions of plume (confluent).

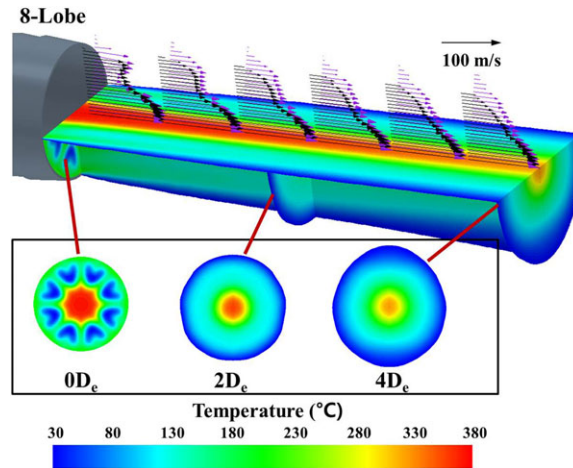


**Figure 20.** Three-dimensional temperature distributions of plume (8-lobe).

the plume ejected from the nozzle exit maintains a concentric temperature distribution, with the high-temperature regions not mixing with each other, and only the size of the high-temperature area gradually decreases. In contrast, for the 8-lobed mixer in Fig. 20, the uneven temperature distribution at the nozzle exit is uniformly mixed at a distance of  $2D_e$  from the nozzle exit. Additionally, the size of the high-temperature area in the centre decreases rapidly, and the temperature of the high-temperature area also decreases. For the 12-lobed mixer shown in Fig. 21, it shows a similar trend to the 8-lobed mixer, but the temperature of the high-temperature area decreases even more rapidly.

Figure 22 shows the transverse velocity of the mixer with respect to the bypass ratio at  $X/L=0.3$ . The transverse velocity ( $\bar{u}_t$ ), excluding the  $X$ -axis velocity ( $u\hat{i}$ ), was used to observe the mixing effect of the transverse flow in detail. The lobe shape allowed the core flow and bypass airflow to create radial velocities in opposite directions. Core gas and bypass air flowed radially outward at the crests and radially inward at the troughs. In the confluent mixer, the transverse velocity at the crest was about 0.5m/s. The transverse velocity at the crest of the 8-lobed and 12-lobed mixers was approximately 10m/s. In the 8-lobed mixer, the transverse velocity at the trough position increased to approximately 4, 5 and 6m/s at bypass ratios of 0.5, 1, and 1.4, respectively. In the 12-lobed mixer, the transverse velocity of the



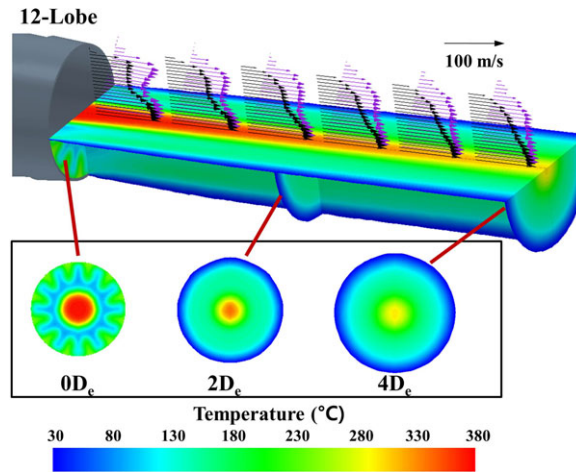


Figure 21. Three-dimensional temperature distributions of plume (12-lobed mixer).

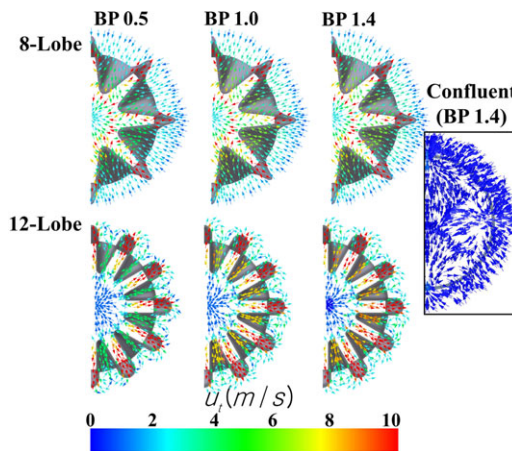


Figure 22. Distribution of transverse velocity vector.

trough position increased to approximately 4, 6 and 8m/s at bypass ratios of 0.5, 1 and 1.4, respectively. Therefore, the transverse velocity is increased with increasing the bypass ratio at the trough position. The mixing rate performance of the core gas and bypass air can be expressed as a rotational motion as follows:

$$\omega_x = \frac{D_e}{u_h} \left( \frac{\partial w}{\partial y} - \frac{\partial v}{\partial z} \right) \tag{19}$$

where  $u_h$  denotes the initial velocity of the core gas at the inlet. Figure 23 shows the vortex distribution inside the nozzle when a lobed mixer was used. Counterclockwise rotational motion is shown in red, and clockwise rotational motion is shown in blue. The two rotations around one lobe channel were in opposite directions. In the figure, as the bypass ratio increased, the rotational motion increased. Therefore, the more lobe channels are present, the more rotational the motion. We believed that the 12-lobed mixer, which has more rotational motion, results in shorter plume temperatures and lengths because the mixing performance is improved.

To estimate the loss values due to mixing, the thrust coefficient was defined. The thrust coefficient is given by thrust coefficient ( $F/F_i$ ), where  $F$  is the thrust value calculated in CFD as  $F_i$  represents the ideal

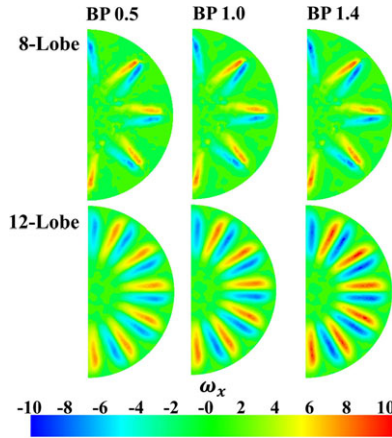


**Figure 23.** *Non-dimensional stream-wise vorticity distributions.*

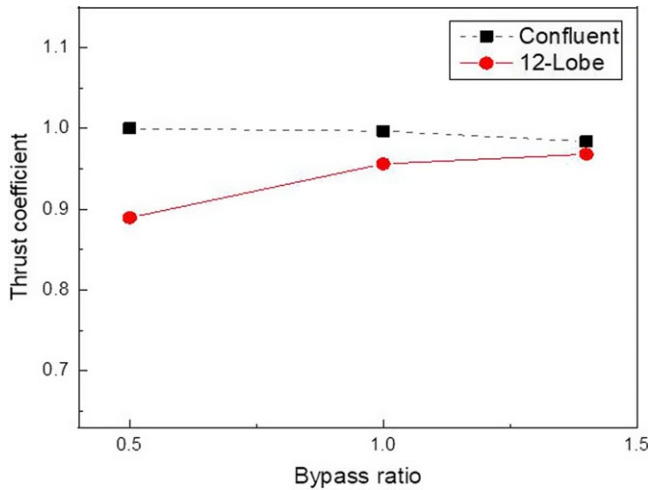


**Figure 24.** *Thrust coefficient with bypass ratio.*

thrust assuming entropy flow. The values of the thrust coefficient according to the bypass are shown in Fig. 24. The figure indicates that the thrust coefficient increases with the increase in bypass ratio when equipped with a lobed mixer, and for a 12-lobed nozzle, as the bypass ratio increases from 0.5 to 1.0 to 1.4, the thrust coefficients are respectively shown to be 0.89, 0.95 and 0.97. Therefore, while equipping a lobed mixer results in benefits from temperature uniformity due to the enhanced mixing effect, it is also evident that there is a significant loss in thrust as a consequence. In this study, it was found that for nozzles equipped with a lobed mixer, a bypass ratio of 1.0 or higher can appropriately achieve the effect of reducing infrared emissions due to the decrease in exhaust gas temperature while minimising thrust loss.

Infrared signal analysis was performed to confirm the infrared signal attributed to the difference in the plume temperature and length caused by the difference in the mixing process. Figure 25 illustrates the infrared signal magnitude for each wavelength band based on the mixer shape. In the infrared signal analysis, we assumed that the observer is behind the nozzle ( $0^\circ$  azimuth angle) and that the bypass ratio is 1.4. The highest infrared signal occurred in the  $\text{CO}_2$  wavelength range of  $4\text{--}4.5\mu\text{m}$ , followed by the  $\text{H}_2\text{O}$  range of  $6\text{--}7\mu\text{m}$ . A comparison of the magnitude of the infrared signal of the

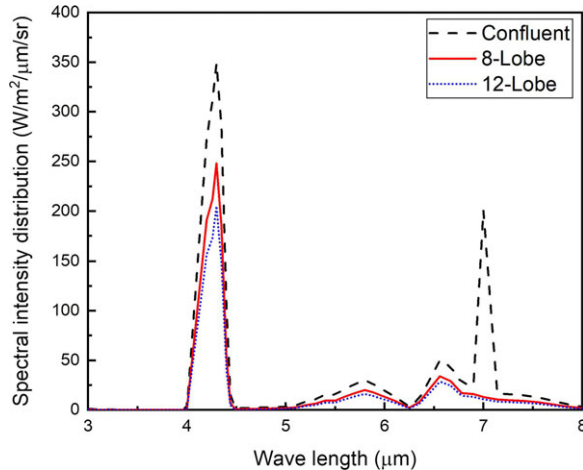


**Figure 25.** *Plume IR signature for various mixer type.*

confluent and lobed mixers showed a tendency consistent with the results of the flow analysis. This is because the lobed mixer has a high mixing rate with the bypass air. Therefore, the temperature of the exhaust gas was lowered, and the high-temperature region was also short-distributed. At all wavelengths, the lobed mixer significantly reduced the infrared signal compared with the confluent mixer, and the 12-lobed mixer reduced the magnitude of the infrared signal more than the 8-lobed mixer. Figure 26 shows the calculation of the maximum infrared signal value in the 3–8  $\mu\text{m}$  band by changing the value by 15° to determine the effect of the mixer shape according to the observation position, and the bypass ratio was 0.5. The highest infrared signal occurred at 0° azimuth, which was directly behind the nozzle, and the infrared signal tended to decrease as it approached 90°. This was because the plume sprayed from the nozzle outlet was concentrated at the centre. The improved mixing performance of the lobed mixer can suppress the infrared signal by approximately 9%–10% compared with the confluent mixer. The maximum infrared signals values at bypass ratios of 1.0 and 1.4 are shown in Figs 27 and 28. We observed that increasing the bypass ratio is effective in reducing the infrared signal at all azimuth angles, and the effect of reducing the infrared signal differed depending on the mixer type. At a bypass ratio of 1, the 8-lobed mixer can suppress the infrared signal of the confluent mixer by a minimum of approximately 9% and a maximum of approximately 40%, depending on the observation position. The 12-lobed mixer system can suppress the infrared signal of the confluent mixer by a minimum of approximately 14% and a maximum of approximately 55%, depending on the observation position. Under the condition of a bypass ratio of 1.4, the 8-lobed mixer can suppress the infrared signal of the confluent mixer by a minimum of approximately 10% and a maximum of approximately 44% depending on the observation position. The 12-lobed mixer system can suppress the infrared signal of the confluent mixer by a minimum of approximately 17% and a maximum of approximately 64%, depending on the observation position. Therefore, the fluid-mixing performance of the mixer has a greater effect on the infrared signal as the bypass ratio increases.

## 5.0 Conclusion

In this study, compressed air was supplied to a micro turbojet engine equipped with a lobed mixer, and the temperature of the plume was measured to determine the mixing performance according to the bypass ratio. Experiments were conducted at bypass ratios of 0.5, 1.0 and 1.4, and plume temperatures were measured at positions 0.16D<sub>e</sub>, 1D<sub>e</sub>, 2D<sub>e</sub>, 3D<sub>e</sub>, 4D<sub>e</sub> and 5D<sub>e</sub> from the nozzle outlet. As a result, the 8-lobed mixer was found to be more effective in lowering the maximum exhaust gas temperature

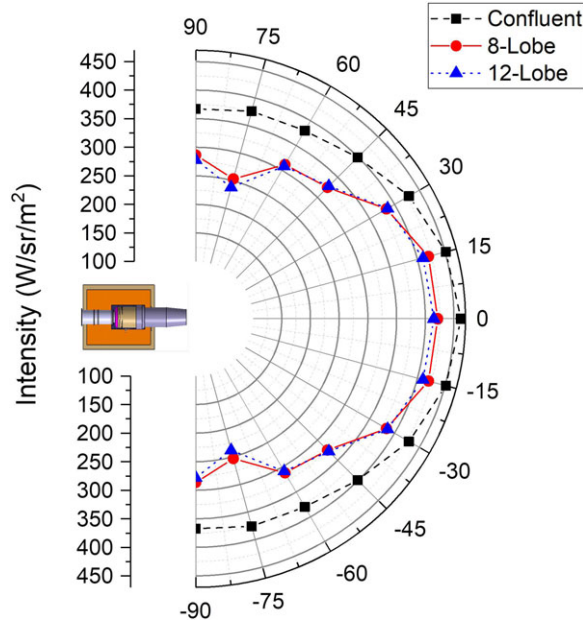


Figure 26. IR signature in the 3–8 $\mu$ m band (bypass ratio = 0.5).

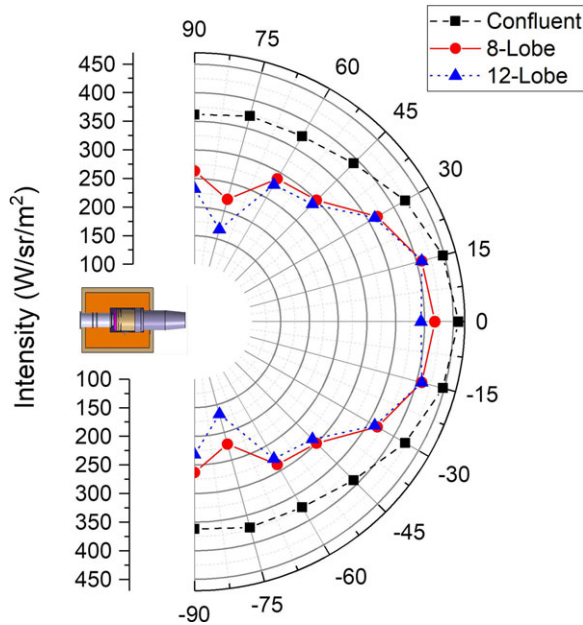


Figure 27. IR signature in the 3–8 $\mu$ m band (bypass ratio = 1.0).

than the confluent mixer. In addition, we found that the higher the bypass ratio, the greater the effect of uniformly mixing the bypass and core air. From the numerical analysis results, we confirmed that the mixing process of the confluent mixer was dominated by free shear flow owing to the difference between the core gas and bypass air velocities. In the case of the lobed mixer, the flow mixing process through transverse flow and rotational motion appeared to be the primary mechanism. In addition, as

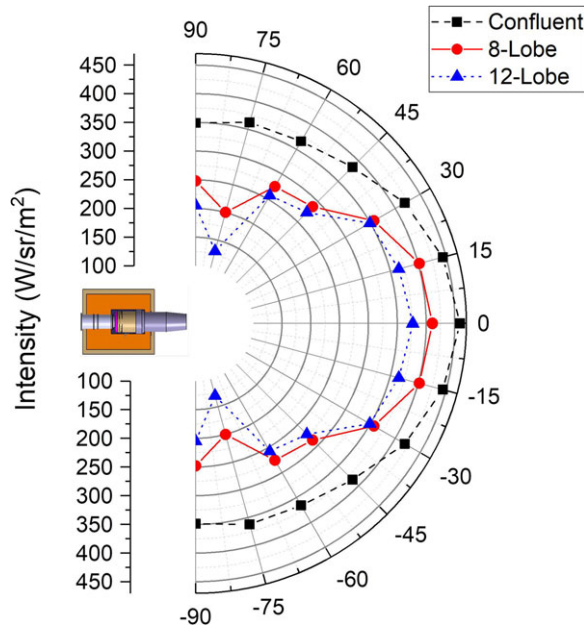


Figure 28. IR signature in the 3–8 $\mu\text{m}$  band (bypass ratio = 1.4).

the number of channels of the lobed mixer increased, the rotational motion increased, which further improved the flow mixing. Furthermore, the improvement in the fluid mixing performance of the mixer was effective in suppressing infrared signals. The infrared signal of the 8-lobed mixer was reduced by 9%, 40% and 44% at bypass ratios of 0.5, 1.0 and 1.4, respectively. The infrared signal of the 12-lobed mixer decreased more than that of the confluent mixer by approximately 10%, 55% and 64% at bypass ratios of 0.5, 1.0 and 1.4, respectively. Through this study, it is possible to understand the mixing characteristics of the flow according to the shape of the mixer at various bypass ratios and determine how they affect the characteristics of the infrared signal. However, the limitation of this study is that the temperature and pressure for bypass flow could not be properly simulated. If research is conducted using an actual turbofan engine in the future, it is expected that the flow characteristics will be more accurately understood.

## References

- [1] Hu, H., Kobayashi, T., Saga, T., Taniguchi, N., Liu, H. and Wu, S. Research on the rectangular lobed exhaust ejector/mixer systems, *Trans. Japan Soc. Aeronaut. Space Sci.*, 1999, **41**, pp 187–194.
- [2] Shan, Y. and Zhang, J.Z. Numerical investigation of flow mixture enhancement and infrared radiation shield by lobed forced mixer, *Appl. Therm. Eng.*, 2009, **29**, pp 3687–3695.
- [3] Choi, S.M., Myong, R.S and Kim, W. Experimental investigation of infrared signal characteristics in a micro-turbojet engine, *Aeronaut. J.*, 2019, **123**, (1261), pp 340–355.
- [4] Choi, S.M., Jang, H.S. and Park, H.H. Infrared signal of the lobed mixer with external air mixing, *Aeronaut. J.*, 2021, **125**, (1291), pp 1501–1518.
- [5] Presz Jr, W.M., Reynolds, G. and McCormick, D. Thrust augmentation using mixer-ejector-diffuser systems, AIAA Paper 1994–0020.
- [6] Paterson, R.W. Turbofan Forced Mixer Nozzle Internal Flowfield, NASA CR-3492, 1982.
- [7] Tew, D.E., Teeple, B.S and Waitz, I.A. Mixer-ejector noise-suppressor model, *J. Propuls. Power*, 1998, **14**, (6), pp 941–950.
- [8] Abolfadl, M.A., Metwally, M.A., El Messiry, A.M and Ali, M.A. Experimental investigation of lobed mixer performance, *J. Propuls. Power*, 2001, **17**, (5), pp 1109–1116.
- [9] Hu, H., Saga, T., Kobayashi, T. and Taniguchi, N. Mixing process in a lobed jet flow, *AIAA J.*, 2002, **40**, (7), pp 1339–1345.
- [10] McCormick, D.C. and Bennett, J.C. Vortical and turbulent structure of a lobed mixer free shear layer, *AIAA J.*, 1994, **32**, (9), pp 1852–1859.

- [11] Merati, P. and Cooper, N.J. Experimental investigation of flow behavior for scalloped and lobed mixers, *Adv. Mech. Eng.*, 2016, **8**, (9), pp 1–17.
- [12] Eckerle, W.A., Sheibani, H. and Awad, J. Experimental measurements of vortex development downstream of a lobed forced mixer, *J. Eng. Gas Turbines Power*, 1992, **114**, pp 63–71.
- [13] Yu, S.C.M and Yip, T.H. Measurements of velocities in the near field of a lobed forced mixer trailing edge, *J. R. Aeronaut. Soc.*, 1997, **101**, pp 121–129.
- [14] Tsui, Y.Y and Wu, P.W. Investigation of the mixing flow structure in multilobe mixers, *AIAA J.*, 1996, **34**, (7), pp 1386–1391.
- [15] Sheng Z.Q., Liu, J.Y and Xu, Y.Y. Mechanisms of lobed jet mixing: About circularly alternating-lobe mixers, *Aerospace Sci. Technol.*, 2020, **98**, (2), p 105660.
- [16] Sheng, Z.Q., Yao, Y. and Xu, Y.H. Suggestions on investigations of lobed jet mixing, *Aerospace Sci. Technol.*, 2019, **86**, pp 415–429.
- [17] Meslem, A., Nastase, I and Abed-Meraim, K. Experimental investigation of the mixing performance of a lobed jet flow, *J. Eng. Phys. Thermophys.* 2008, **81**, (1), pp 106–111.
- [18] Lockwood, F.C. and Shah, N.G. A new radiation solution method for incorporation in general combustion prediction procedures, *Symp. Combust.*, 1981, **18**, (1), pp 747–760.
- [19] Cheng, W., Wang, Z., Zhou, L. and Sun, X. Infrared signature of serpentine nozzle with engine swirl, *Aerospace Sci. Technol.*, 2019, **86**, pp 794–804.
- [20] Decher, R. Infrared emissions from turbofans with high aspect ratio nozzles, *J. Aircraft*, 1981, **18**, (12), pp 1025–1031.
- [21] Liu, Y.H. Experimental and numerical investigation of circularly lobed nozzle with/without central plug, *Int. J. Heat Mass Transf.*, 2002, **45**, (12), pp 2577–2585.
- [22] Elliott, J., Manning, T., Qiu, Y., Greitzer, E., Tan, C. and Tillman, T. Computational and experimental studies of flow in multi-lobed forced mixers, AIAA Meeting paper 28th Joint Propulsion Conference and Exhibit, 06 July 1992–08 July 1992.
- [23] Barber, T., Paterson, R.W. and Skebe, S.A. Turbofan forced mixer lobe flow modeling experimental and analytical assessment, NASA Contractor Report 4147.
- [24] Zografos, A.I., Martin, W.A. and Sunderland, J.E. Equations of properties as a function of temperature for seven fluids, *Comput. Methods Appl. Mech. Eng.*, 1987, **61**, (2), pp 177–187.
- [25] Mahulikar, S.P., Rao, G.A., Sane, S.K. and Marathe, A.G. Aircraft plume infrared signature in nonafterburning mode, *J. Thermophys. Heat Transf.*, 2005, **19**, (3), pp 413–415.
- [26] An, C.H., Kang, D.W., Baek, S.T., Myong, R.S., Kim W.C. and Choi S.M. Analysis of plume infrared signatures of S-shaped nozzle configurations of aerial vehicle, *J. Aircraft*, 2016, **53**, (6), pp 1768–1778.
- [27] Lee, H.J, Myong, R.S., Choi, S.M. and Kim, W.C. Computational investigation of nozzle flowfield in a microturbojet engine and its scaling characteristics, *J. Comput. Fluids Eng.*, 2017, **22**, (1), pp 43–50.
- [28] Xie, Y., Zhong, C., Ruan D.F., Liu, K and Zheng B. Effect of core flow inlet swirl angle on performance of lobed mixing exhaust system, *J. Mech.*, 2016, **32**, (3), pp 325–337.
- [29] Hu, H., Kobayashi, T., Saga, T., Segawa, S. and Taniguchi, N. Particle image velocimetry and planar laser-induced fluorescence measurements on lobed jet mixing flows, *Exp. Fluids*, **29**, (7), pp 141–157.
- [30] Sheng, Z.Q., Chen, S.C., Wu, Z and Huang, P.L. High mixing effectiveness lobed nozzles and mixing mechanisms, *Sci. China*, 2015, **58**, (7), pp 1218–1233.